


Article

SnSe₂-Zn-Porphyrin Nanocomposite Thin Films for Threshold Methane Concentration Detection at Room Temperature

Adam Lőrinczi ^{1,*}, Eugenia Fagadar-Cosma ^{2,*} , Gabriel Socol ³ , Andreea Mihăilescu ³, Elena Matei ¹ , Florinel Sava ¹ and Mariana Ștefan ¹ 

¹ National Institute of Materials Physics, 405A Atomistilor St., RO-077125 Magurele, Romania; elena.matei@infim.ro (E.M.); fsava@infim.ro (F.S.); mstefan@infim.ro (M.Ș.)

² “Coriolan Dragulescu” Institute of Chemistry of Romanian Academy, Mihai Viteazul Ave., No. 24, 300223 Timisoara, Romania

³ National Institute for Laser, Plasma and Radiation Physics, 409 Atomistilor St., RO-077125 Magurele, Romania; gabriel.socol@inflpr.ro (G.S.); andreea.mihailescu@inflpr.ro (A.M.)

* Correspondence: lorinczi@infim.ro (A.L.); efagadar@yahoo.com (E.F.-C.); Tel.: +40-21-369-0185 (A.L.); +40-256-491-818 (E.F.-C.)

Received: 29 October 2020; Accepted: 15 December 2020; Published: 18 December 2020



Abstract: Nanocomposite thin films, sensitive to methane at the room temperature (25–30 °C), have been prepared, starting from SnSe₂ powder and Zn(II)-5,10,15,20-tetrakis-(4-aminophenyl)-porphyrin (ZnTAPP) powder, that were fully characterized by XRD, UV-VIS, FT-IR, Nuclear Magnetic Resonance (¹H-NMR and ¹³C-NMR), Atomic Force Microscopy (AFM), SEM and Electron Paramagnetic Resonance (EPR) techniques. Film deposition was made by drop casting from a suitable solvent for the two starting materials, after mixing them in an ultrasonic bath. The thickness of these films were estimated from SEM images, and found to be around 1.3 μm. These thin films proved to be sensitive to a threshold methane (CH₄) concentration as low as 1000 ppm, at a room temperature of about 25 °C, without the need for heating the sensing element. The nanocomposite material has a prompt and reproducible response to methane in the case of air, with 50% relative humidity (RH) as well. A comparison of the methane sensing performances of our new nanocomposite film with that of other recently reported methane sensitive materials is provided. It is suitable for signaling gas presence before reaching the critical lower explosion limit concentration of methane at 50,000 ppm.

Keywords: SnSe₂; Zn-metalloporphyrin; thin film; room temperature; resistive sensor; methane detection

1. Introduction

Methane (CH₄) is well known as an odorless gas, and as flammable and combustible in the presence of oxygen. It is one of the components of natural gas and has multiple applications, such as mining, oil and gas operations or home safety. The lower explosion limit (LEL) of methane is 5.0 vol.%, which corresponds to 50,000 ppm.

The classical and versatile SnO₂ gas sensing material was initially developed by researchers from Japan several decades ago [1]. Generally, the gas sensing material is deposited onto planar interdigitated electrodes (IDEs), or onto some functionally equivalent structure, such as coils or meshes. The back side of the IDEs are provided, in most cases, with a continuous electrode for heating, to allow the setting of the working temperature of the sensor, against a given gas which we want to detect.

Many research groups worldwide are working intensely in the field of gas sensing materials to improve performances [2] or to find new compositions suitable for gas sensing [3–8]. A review on the principles, operation, and developments of gas sensors is given by the contributing authors in

the book edited by Sberveglieri [9]. Metal oxides such as SnO₂ or ZnO [1,8,10–15] are versatile and ubiquitous for methane sensing, but trends focusing on graphene [16–20] or metal-organic frameworks (MOFs) [21–25] emerge as possible alternatives to ensure lower operating temperature ranges.

Notably there is an obvious general interest to find alternative gas sensing materials to SnO₂, which needs to be heated up to working temperatures of 200–600 degrees Celsius. The high value for the operating temperature is a serious drawback in the case of remote in-field applications, where energy supplies for heating the sensor might not be easily available. At the same time, the need for a bulky battery to keep the sensor heated-up to the sensing materials' operating temperature will also hinder the down scaling of the gas sensor. Under these circumstances, room temperature (RT) sensing materials are highly desired, and a focused effort is invested worldwide to identify them.

In this work we present and characterize a new nanocomposite material, based on a chalcogenide compound, SnSe₂, and a metalloporphyrin, which shows a prompt and systematic response to the presence of methane (CH₄) at a concentration as low as 1000 ppm in synthetic dry air, as well as in air with 50% RH at room temperature (~25–30 °C), and which has a simple way of preparation even at a larger scale [26]. Excellent selectivity for NO₂, with respect to NH₃, was recently achieved by the gas sensors also based on an anisotropic binary-layered SnSe₂ material. This selectivity is due to charge transfer and the mobility of the flat band, induced from the adsorption of gases [27]. Sensing tests performed using other type of heterostructures SnO₂/SnSe [28] at a temperature of 150 °C provided excellent sensitivities of (1.06 ± 0.03) and (0.43 ± 0.02) ppm⁻¹ for NO₂ and H₂, respectively, in dry air.

The works of Popescu and co-authors [29,30] mark the inception of gas sensitivity investigations of SnSe₂ thin films for methane. A more comprehensive analysis of the structural, morphological, optical, and the sensing properties of tin selenide thin films as a methane sensing material can be found in [31], while the most recent report on the topic [32] describes a co-evaporation technique as a way of achieving single-crystalline, self-standing SnSe₂ nanoplate arrays on flexible polyimide substrates, and their subsequent deployment in wearable CH₄ sensors.

Porphyrins are tetrapyrrolic macrocycles with an extended π -aromatic conjugation, exhibiting unusual optical and electrical properties, and high chemical and conformational versatility [33]. The four pyrrolic nitrogens enable the easy binding of almost all of the metal ions to form metalloporphyrins, a class of compounds known for their ability to selectively attach to various gas molecules. In addition, the electron donor or acceptor nature of peripheral substituents influences the binding affinity of the axial ligands to the metal centers, hence impacting the metalloporphyrin's reactivity to gases. Such peculiar properties have triggered various new developments as well as significant improvements in the design of chemical sensors [34–37], but the field of porphyrins-based gas sensing remains insufficiently explored. In this sense, the work of Ngo et al. [38] offers some insights into the influence of the central metals on the sensing mechanisms.

The binding mechanism might be explained by axial coordination to the metal ion in the centre of porphyrin, or by van der Waals forces, hydrogen bonding, or by π – π interactions of peripheral substituents with the guest molecules [33], and in each case the binding process is accompanied by changes in optical, electrical, or conformational properties [36].

In addition, the electron donating or withdrawing nature of peripheral substituents led to modifications of the binding affinity of axial ligands to metal centers. In order to better understand the role of metals in the mechanism of metalloporphyrin-based gas sensing, a study was done by eliminating the effects of peripheral substituents, using only porphine and metalloporphines [38]. It is remarkable, that a free-base porphyrin, covalently bonded to a networked silica structure, was efficient for acetone vapors sensing [39].

Recent chemical synthesis and material studies address hybrid nanostructured materials, incorporating porphyrins or metalloporphyrins, bound to either silica [39,40] or to carbon nanotubes [41,42]. These compositions are suitable to detect acetone vapors [39], H₂O₂ [40], NO₂ [41,42], or volatile organic compounds (VOCs) [43–50], respectively. A₃B porphyrin-based compounds [51–53] are known for their suitability in CO₂ sensing, while increasingly more porphyrin derivatives and porphyrin containing

networks emerge as new sensing materials for trace O_2 [54], Cl_2 [55], NH_3 [56,57], various VOCs [58–60], or explosives in gas phase [61,62].

All of the above studies reveal that through a skillful chemical customization of the porphyrins-based material in its synthesis stage, it is possible to make the sensor sensible towards specific analyte gases and, therefore, a precise tuning of the gas sensor's selectivity may be attained. Moreover, the good carrier mobility of the $SnSe_2$ nanocrystals, along with an appropriate metalloporphyrin, makes them attractive for gas sensing composites formation.

As of our knowledge, in spite of all advances so far, studies on the gas sensitivity of hybrid composites based on tin selenide and metalloporphyrin complexes have not yet been reported. In this sense, our paper aims to offer valuable insights on the subject by introducing a new methane-sensitive nanocomposite material, consisting of both $SnSe_2$ and $Zn(II)$ -5,10,15,20-tetrakis-(4-aminophenyl)-porphyrin (ZnTAPP). The proposed composite was subject to thorough material investigations, as well as to extensive testing in controlled CH_4 atmospheres, and was found to be highly suitable for deployment in low-cost conductometric sensors.

2. Materials and Methods

In order to prepare the new methane-sensing nanocomposite material we have partly used commercially available high purity solvents, as well as materials synthesized in our laboratories, like the $SnSe_2$ ingot and the $Zn(II)$ -porphyrin powder, as described below.

2.1. $SnSe_2$ Preparation and X-ray Testing

The starting powder has been prepared from small pure Sn bar pieces and pure Se pellets, by melting the appropriate amount of both substances in a quartz ampoule, which has been sealed under vacuum. The synthesis process took place in a rocking furnace, at a temperature around 700 °C, for two hours. The melt has been cooled down in the ampoule, and the $SnSe_2$ powder has been obtained from the cooled-down ingot. The powder sample has been measured by X-ray diffraction (XRD) with the $Cu_{K\alpha}$ radiation on a Bruker D8 Advance diffractometer, in order to check the formation of the $SnSe_2$ compound. Figure 1 shows that our powder is polycrystalline $SnSe_2$.

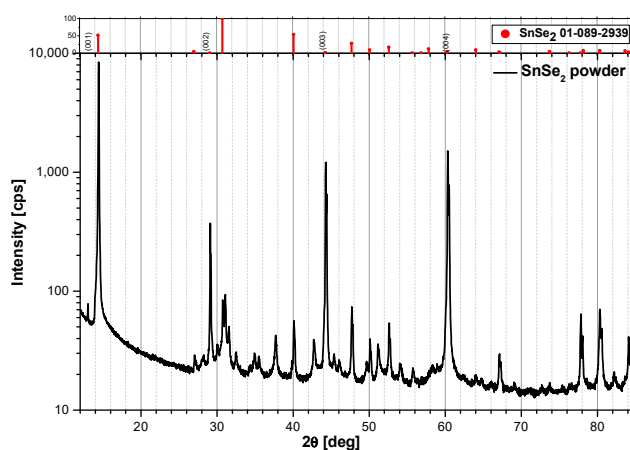


Figure 1. XRD diagram for the $SnSe_2$ powder.

2.2. Zn-Porphyrin Synthesis

The synthesis of $Zn(II)$ -5,10,15,20-meso-tetrakis-(*p*-amino-phenyl)-porphyrin, was done in three steps, involving the obtaining of 10,15,20-meso-tetrakis-(*p*-nitro-phenyl)-porphyrin, followed by the reduction in nitro-groups with $SnCl_2$ [63], and finally by metalation reaction with Zn salt [64]. All of the reagents used in this work have been provided by Sigma-Aldrich and Merck and were purum analiticum grade.

2.2.1. Obtaining of 5,10,15,20-Meso-Tetrakis-(*p*-nitrophenyl)-Porphyrin

A mixture containing 0.44 g (2.8 mmol) *p*-nitrobenzaldehyde and 0.5 mL (5.33 mmol) acetic anhydride was added to 15 mL propionic acid, and brought to reflux under vigorous stirring in a nitrogen gas atmosphere. In the next step, 1 mL of propionic acid, containing 0.20 g (2.8 mmol) pyrrole, was added to the mixture and refluxed for 30 min under stirring. The tarry solution was slowly cooled and kept for 24 h.

The dark solid was separated by filtration, six times washed with 10 mL portions of H₂O, and dried under vacuum. The powdery solid was mixed with 5 mL of pyridine, refluxed under stirring for 1 h, cooled to room temperature, and then stored at −4 °C overnight. The mixture was filtered and repeatedly washed with acetone to finally yield 150 mg (22%) of 5,10,15,20-meso-tetrakis-(*p*-nitro-phenyl)-porphyrin.

2.2.2. Obtaining of 5,10,15,20-Meso-Tetrakis-(*p*-aminophenyl)-Porphyrin (TAPP)

A solution of 150 mg (0.18 mmol) 5,10,15,20-meso-tetrakis-(*p*-nitro-phenyl)-porphyrin in 10 mL concentrated HCl was bubbled with Ar for 1 h. A solution of 0.675 g (3 mmol) SnCl₂ · 2H₂O in 2 mL of concentrated HCl, also bubbled with Ar, was added to the porphyrin solution.

The resulting mixture was stirred and heated in a water bath (75–80 °C) for 30 min. The hot-water bath was carefully replaced with a cold-water bath and then an ice-bath (−5 °C). The reaction mixture was then neutralized under Ar by slow addition of 10 mL of concentrated NH₄OH, taking care to keep the exothermic reaction under control. The resultant basic solution was exposed to air, filtered, and the solid was vigorously stirred with 15 mL of 5% NaOH.

The obtained solid was again filtered, washed with water, dried, and then extracted using Soxhlet apparatus with 20 mL of CHCl₃. The volume of the purple solution was reduced by rotary evaporation, and after the addition of 10 mL EtOH and the last evaporation, gave dark-green crystalline tetra-(*p*-amino-phenyl)-porphyrin, TAPP, yield about 75 mg (49%).

The structure of TAPP (Figure 2) was confirmed by (¹H NMR), (¹³C NMR), FT-IR and UV-VIS spectroscopy.

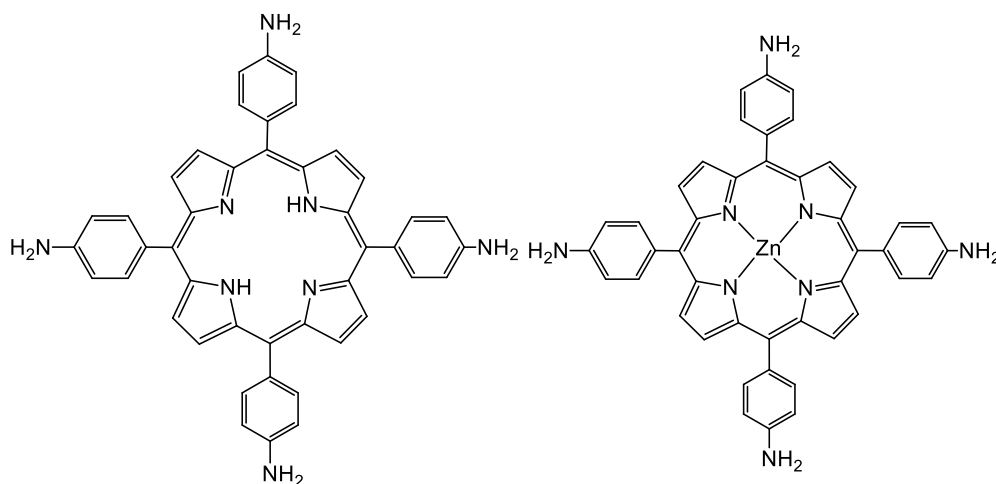


Figure 2. The chemical structures of TAPP and of ZnTAPP.

2.2.3. Synthesis of ZnTAPP

A solution comprising 75 mg TAPP (0.11 mmol) dissolved in 70 mL CHCl₃ was brought to reflux and 156 mg (0.93 mmol) Zn(CH₃COO)₂ dissolved in 3 mL of methanol were added under N₂ atmosphere and refluxed for 4 h at 65 °C. After completion of the reaction, monitored by UV-VIS spectroscopy, the solvent was removed, the excess of Zn salt was thoroughly washed with double distilled water and the product was purified by recrystallization in CHCl₃ (yield, 87%).

The compound ZnTAPP, was also represented in Figure 2 and was characterized by FT-IR and UV-VIS spectroscopy, respectively.

2.3. Characterization of the Synthesized Tapp and Zntapp Porphyrins

The NMR spectra were performed on a Bruker 400 MHz spectrometer (Germany) and using dimethyl sulfoxide (DMSO)-d₆ as solvent. Chemical shifts (δ) are revealed in ppm downfield from the internal standard tetramethylsilane. UV-VIS spectra were recorded on a JASCO UV-V-650 spectrometer (Pfungstadt, Germany), using standard 1 cm pass cells. Atomic force microscopy (AFM) images were performed on a Nanosurf[®] EasyScan 2 Advanced Research AFM (Amsterdam, The Netherlands) at room temperature, with samples drop-casted from THF on silica plates in noncontact mode. FT-IR spectra were registered on a JASCO 430 apparatus as KBr pellets.

Electron paramagnetic resonance (EPR) investigations in the X (9.87 GHz) and Q (34.1 GHz) frequency bands were carried out on Bruker ELEXSYS-E580 and ELEXSYS-E500Q spectrometers, respectively. Two porphyrin samples in powder form were inserted into calibrated 2 mm i.d./3 mm o.d. pure silica tubes. The EPR spectra were recorded at room temperature (RT). The determination of the EPR parameters and lineshape simulation of the spectra were performed with the EasySpin v. 5.2.16 program [65].

2.3.1. UV-VIS Spectroscopy

From the UV-VIS spectroscopy (Figure 3), it can be observed that the Soret band of the Zn-metallated compound is bathochromically shifted to 433 nm, as compared to the one for the free base porphyrin, located at 424 nm. A splitting of its Soret band is also noted, the second peak being less intense and located at 394 nm, this is an indicative of a slight H-type process of aggregation.

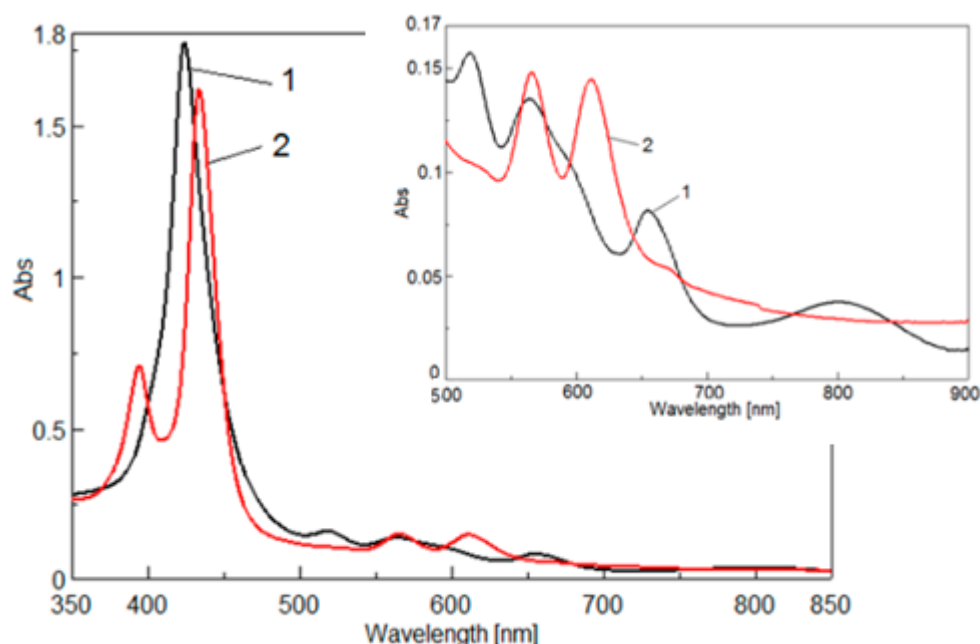


Figure 3. Overlapped UV-VIS spectra of 5,10,15,20-tetrakis-4-aminophenyl-porphyrin (1) and its Zn-metallated derivative (2) solved in DMSO; detail of the Q bands.

The Q bands of the ZnTAPP, located at 566 nm and at 611 nm, manifest a hyperchromic effect in comparison with the Q bands of porphyrin-base, and are reduced from 4 in TAPP to only 2 in ZnTAPP, showing an increase in symmetry. The symmetry of the ZnTAPP is changed from D_{2h} to D_{4h}, the cleavage degree of the molecular orbital decreases and the degeneracy increases. As a consequence, the number of Q bands decreases.

2.3.2. FT-IR Spectroscopy

In the FT-IR spectra (Figure 4), all compounds revealed a large absorption band around $3300\text{--}3500\text{ cm}^{-1}$ for the stretching vibration of N-H bond, at 1583 cm^{-1} for ZnTAPP and located at 1599 cm^{-1} for TAPP, as typical bending vibrational band of the porphyrin group. Beside these frequencies, the absorption bands belonging to C=N, C=C appeared around $1705\text{--}1710\text{ cm}^{-1}$ and $1405\text{--}1465\text{ cm}^{-1}$, respectively. In addition, the presence of vibrational absorption band at 996 cm^{-1} was assigned previously for Zn-N [66], and is a proof for the proper synthesis of the metalloporphyrin.

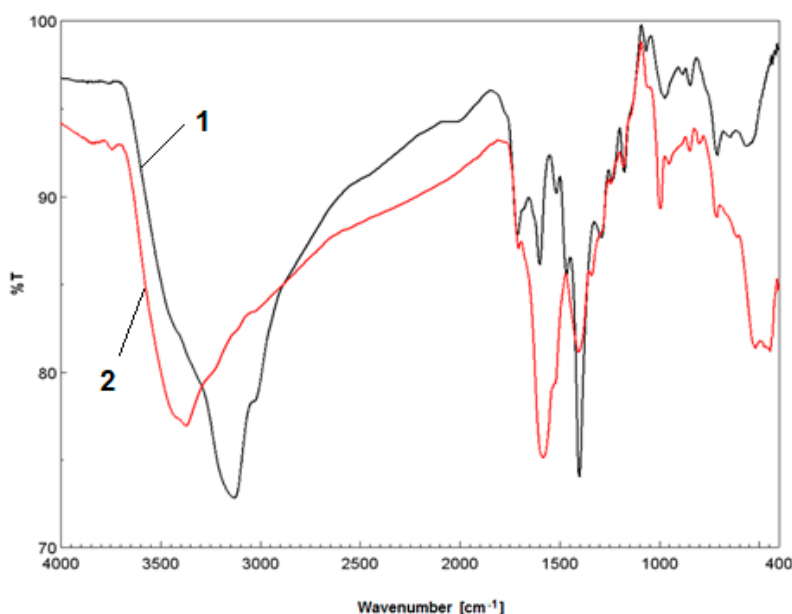


Figure 4. Overlapped FT-IR spectra of 5,10,15,20-tetrakis-4-aminophenyl-porphyrin (1) and its Zn-metallated derivative in KBr pellets (2).

TAPP: FT-IR: (KBr), cm^{-1} : 3130 (NH stretching), 1599 (N-H deformation and ν C=C Ph), 1465 (C=C aromatic), 1400 (ν C=N), 1176 (δ C-H Ph), 1066 (δ C-H Ph), 709 (γ C-H Ph); ^1H NMR (DMSO- D_6); δ ppm: 8.91 (bs, 8H, β pyrrole), 7.82–7.88 (d, 8H, meta positioned protons to the NH_2), 7.04–7.06 (d, 8H, ortho positioned protons to the NH_2), 4.11–4.33 (d, 8H from NH_2), -2.78 (s, 2H, inner NH-porphyrin ring); ^{13}C NMR (DMSO- d_6); δ ppm: 131.51, 128.54, 112.41; UV-VIS. λ_{max} (in DMSO, nm, (log ϵ)): Soret: 424 (5.24), Q bands: 518 (4.19), 564 (4.12), 654 (3.90), 801 (3.53).

In the ^1H NMR spectrum of the symmetrical porphyrin TAPP, the inner N-H pyrrole signal is present at -2.78 ppm. In the aromatic region, there are two doublets, at 7.82–7.88 corresponding to the eight phenyl protons in the meta position and at 7.04–7.06 assigned to the eight aromatic protons in the ortho position. The eight β pyrrole protons are equivalent and manifest as a singlet signal at 8.91 ppm. The chemical shift (δ) of ^{13}C NMR is reduced to the presence of the meso carbons which are resonating at 112 ppm, and of the β -pyrrolic carbons which are resonating in the range of 128–131 ppm.

ZnTAPP: FT-IR: (KBr) cm^{-1} : 3372 (N-H, str.), 1583 (N-H deformation), 1405 (C=C, aromatic), 1180 (δ C-H Ph), 996 (Zn-N), 848 and 712 (γ C-H Ph), 445 (ν Zn-N); UV-VIS. λ_{max} (in DMSO, nm, (log ϵ)): Soret: 433 (5.20) (shoulder at 394 (4.84)), Q bands: 566 (4.16), 611 (4.15).

2.3.3. EPR Spectroscopy

The EPR spectra of the two porphyrin powder samples measured in the Q-frequency band are displayed in Figure 5.

Similar features, such as the lines characteristic to isolated Cu(II) ions, present as native impurities, can be observed in both samples. Based on the spectra intensity, the concentration of the Cu(II) ions is less than 1×10^{16} ions/mg. This Cu(II) spectrum is very similar with the spectra observed in other

copper porphyrin complexes, where the Cu(II) ions are coordinated by four nitrogen atoms in a square planar configuration [67]. Indeed, as shown in the detailed view from Figure 6, the high-field part of the spectrum displays a complex structure due to the superhyperfine interaction with four nitrogen ^{14}N nuclei. A good simulation of the Cu(II) spectrum was obtained with the axial EPR parameters $g_{\parallel} = 2.188 \pm 0.001$, $g^{\perp} = 2.047 \pm 0.001$, $A_{\parallel}^{\text{Cu}} = (197 \pm 1) \times 10^{-4} \text{ cm}^{-1}$, $A_{\perp}^{\text{Cu}} = (30 \pm 1) \times 10^{-4} \text{ cm}^{-1}$, $A_{\parallel}^{\text{N}} = A_{\perp}^{\text{N}} = (16 \pm 1) \times 10^{-4} \text{ cm}^{-1}$ and a Gaussian line shape with peak-to-peak linewidth $\Delta B = 1.5 \text{ mT}$ (see Figure 6).

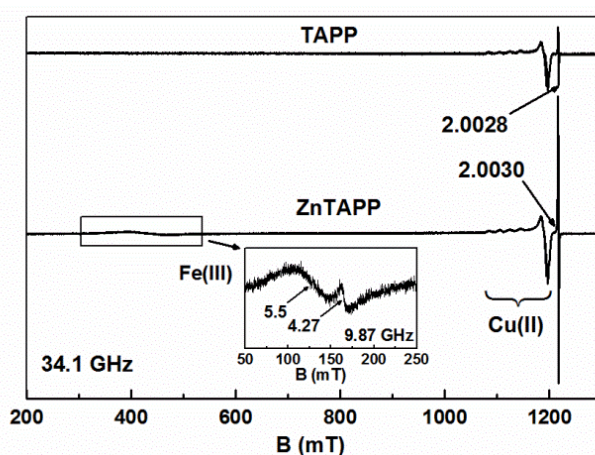


Figure 5. Q-band EPR spectra of the TAPP (top) and ZnTAPP (bottom) samples measured at RT. Inset: detailed view of the Fe(III) signals in the X-band EPR spectrum of the ZnTAPP sample.

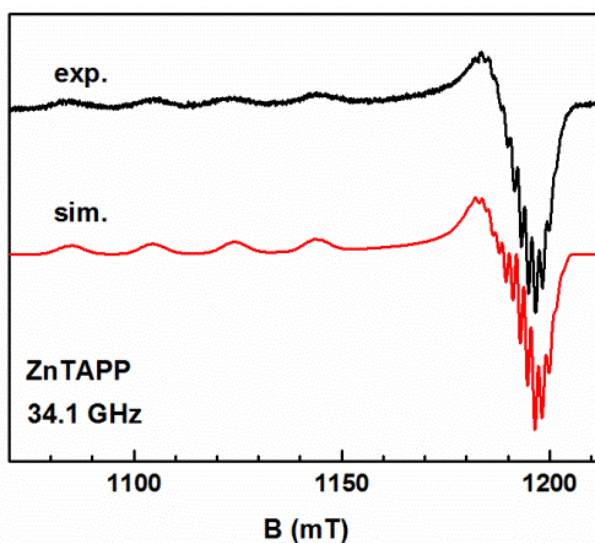


Figure 6. Q-band EPR experimental (top) and simulated (bottom) spectra of the Cu(II) ions in the ZnTAPP sample.

The broad line observed around 450 mT in the Q-band ZnTAPP spectrum (Figure 5) is very probably due to isolated Fe(III) ions present as native impurities in a very low concentration. This assignment is supported by the two lines observed in the X-band spectrum at the effective g -values 4.27 and 5.5, respectively (Figure 5, inset), which could be ascribed to a Fe(III) complex with a $S = 5/2$, $3/2$ spin admixed ground state [68].

A slightly asymmetric line can also be observed at $g \sim 2.0028$ in TAPP and $g \sim 2.0030$ in ZnTAPP, respectively (Figure 5), with a peak-to-peak linewidth $\Delta B \sim 1.0 \text{ mT}$, originating most probably from some radicals. The intensity of this line is four times larger in the ZnTAPP sample than in the TAPP sample. It is very possible that these stable radicals observed in the EPR spectra of the two samples,

characterized by different g-values and intensities, are associated with different cations, such as: Cu^{2+} or Fe^{3+} , present as native impurities in the Sn and Zn salts used in metalation reaction for obtaining of TAPP porphyrin base and its Zn-metalloporphyrin, respectively.

2.3.4. Surface Morphology Characterization by AFM Microscopy

As already expected from the UV-VIS spectra that showed some H-type aggregation phenomena regarding the ZnTAPP, the AFM images (Figure 7a,b) proved a stronger aggregation in the case of metallated compounds. The defined architecture of triangular shape formed in TAPP (Figure 7a) is changed into a kvatarons-type structure [69], of larger aggregates (Figure 7b), obtained by hydrophobic interactions.

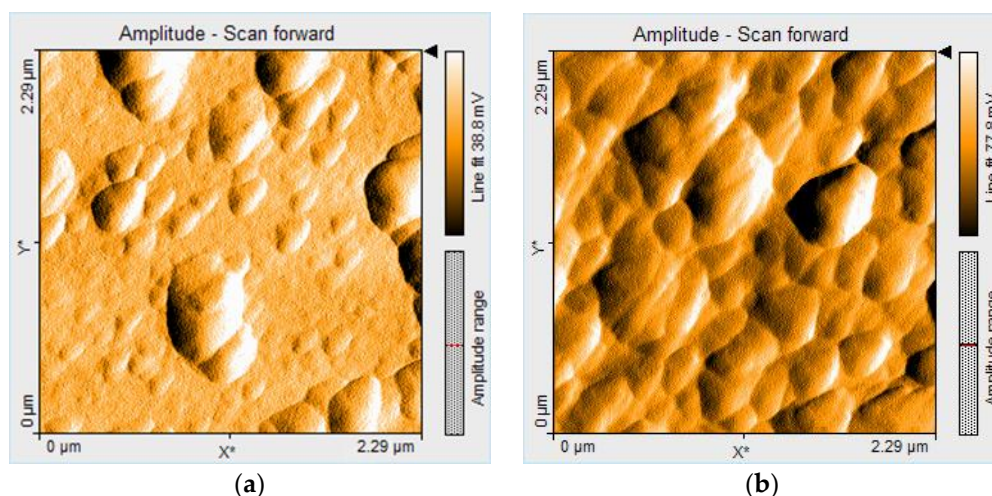


Figure 7. 2D AFM images of TAPP (a) its ZnTAPP derivative (b) and from THF solvent

2.4. Nano-Ccomposite Thin Film Preparation

As starting materials we used SnSe_2 and $\text{Zn(II)-5,10,15,20-tetrakis-(4-aminofenil)-porphyrin}$, both in powder form. They were dissolved in amine- and methyl-containing solvents [70], in concentrations of 10^{-3} – 10^{-2} mol/L. The two obtained solutions were labelled with S for SnSe_2 and with ZP for the ZnTAPP. We ultrasonically mixed the two solutions, and the resulting solution we have labelled with SZP. From this final solution we have drop casted, with an Eppendorf 200 analytical pipette, about 30 micro-liters onto an interdigitated sensor support.

The samples, obtained as previously described, have been dried in an oven for 60–100 min, at 60–80 °C, resulting in a continuous and uniform thin grey layer, which covered well the interdigitated electrodes (Figure 8).



Figure 8. The thin nanocomposite layer after drop casting and drying on the sensor support with IDEs.

The surface morphology of the SnSe_2 and Zn-metalloporphyrin powder precursors, and the final gas sensing nanocomposite, have been studied by scanning electron microscopy (SEM), and are resented in Figure 9a–c. The film thickness was estimated from an SEM image taken in side view. It was found to be around 1.3 micrometers.

Let us observe that SnSe_2 shows a fragmented polycrystalline surface (Figure 9a), while the Zn-porphyrin features a spongeous-like network surface structure with smaller structural motifs

(Figure 9b). The surface arrangement of porphyrins induces modifications in the sensitivity, with respect to the non-aggregated porphyrins [71,72]. On Figure 9c one may see how the first two structures form our new nanocomposite, where the finer Zn-porphyrin covers the coarse SnSe₂ polycrystalline surface features. The merge of these two precursor structures with different rugosities proves to yield a nanocomposite with enhanced gas sensing ability for methane, compared to the very poor responses of the precursors tested individually.

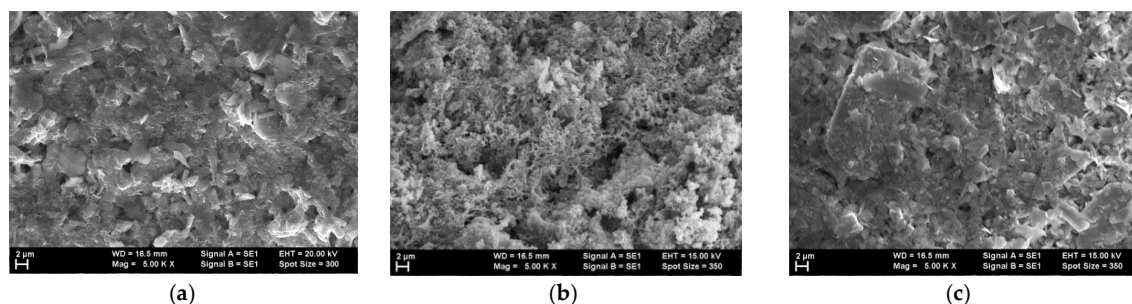


Figure 9. (a) Image of SnSe₂ powder. (b) Image of the ZnTAPP powder. (c) Image of the SZP nanocomposite.

2.5. Testing The Sensor Material for Methane at Room Temperature

The resulting sensor was introduced in a designated testing chamber and kept completely isolated from the external environment for the whole duration of the test. Although, the temperature and pressure conditions inside the chamber can be strictly controlled and monitored, the SZP thin film sensor performed outstandingly at room temperatures of 23–28 °C.

The testing protocol implies applying an electrical current to the sensor and measuring the voltage variations, a simple but reliable method of deriving the behavior of its electrical resistance in the presence of an analyte gas. For this purpose, we used a source measure unit (SMU), a Keithley SMU 2450, connected directly to the gas chamber and, in the particular case of the SZP, it was determined that 1 µA is an optimal test current. The analyte gas—the methane—was introduced in the chamber in a pre-established concentration (1000 ppm) and at well set time intervals (10 min), through the designated Alicat Scientific mass flow controllers that regulate the gas flow to the test chamber. The testing protocol requires for the analyte to be alternated with a gas to which the sensor is insensitive, namely dry synthetic air, in order to prove the reproducibility of the sensor's response to methane. We maintained the synthetic air alternations for the same duration of 10 min. This cycle has been repeated for about ten times. The variation of the resistance during this test is given in Figure 10 below.

One can observe, on Figure 10, that the methane sensing film has a reproducible, prompt and systematic response to the presence of the methane: as 1000 ppm methane is added to the flowing dry air, the value of the electrical resistance of the film suddenly begins to drop sharply. As soon as the methane flux is stopped, the value of the electrical resistance begins to grow, again very sharply. The magnitude of the resistance's relative drop upon the presence of the methane, and the magnitude of the relative increase in the resistance as the methane flux is stopped is around 5%.

To simulate on-site real air composition, controlled 50% relative humidity conditions were attained using a controlled evaporation and mixing (CEM) unit, model Bronkhorst part of the gas sensors testing facility. The CEM-System consists of a thermal liquid flow controller, a mass flow controller for the carrier gas, and a temperature controlled mixing and evaporation device. The resident CEM is suitable for mixing liquid flows up to 30 g/h, resulting in saturated vapor flows of up to 4 L/min. The sensor's responses to 1000 ppm of CH₄ in controlled 50% relative humidity conditions are given in Figure 11.

We can notice from Figures 10 and 11, that the presence of 50% RH in the testing air results in a roughly 2.5 times lower response magnitude of the nanocomposite to methane, but the shape of the response preserves its periodicity, following the on and off switching of the methane promptly.

This response is suitable as an input to an electronic signal processor and analyzer unit for various application purposes.

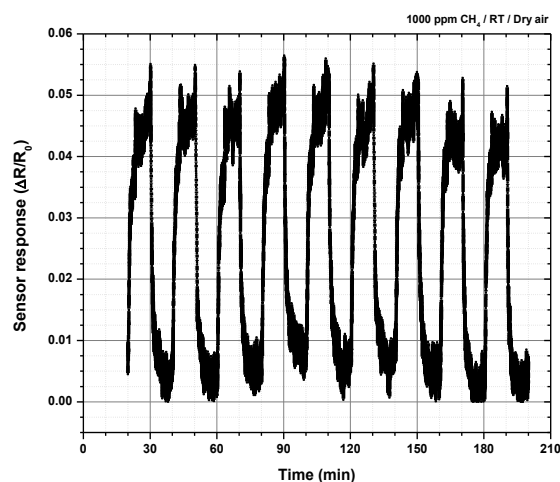


Figure 10. Response of the sensor to 1000 ppm methane in dry air at RT. Measuring cycle: 10 min air flow, followed by 10 min air + 1000 ppm methane flow. Cycle begins at $t = 20$ min.

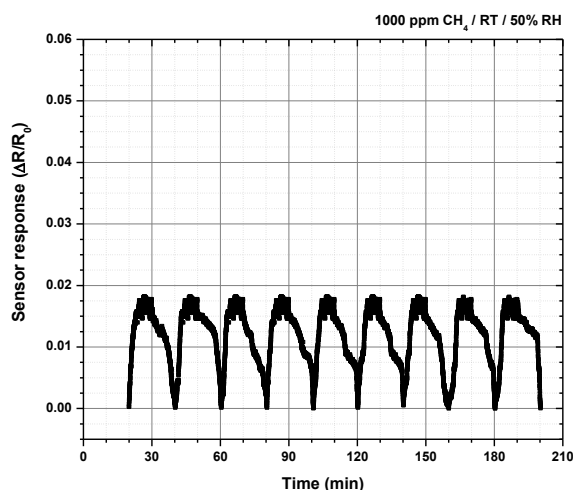


Figure 11. Response of the sensor to 1000 ppm methane in humid air at RT. Measuring cycle: 10 min humid air flow, followed by 10 min humid air + 1000 ppm methane flow. Cycle begins at $t = 20$ min.

This sensing material reacts to the presence or absence of methane through changing not only the value of the equivalent resistance, but also the slope's sign. For the later we have a very quick time response, of about 5–10 s, having a non-linear decrease. From Figure 11 we can see that the slope of the curve changes almost instantly from slightly positive to steeply negative, as methane contacts the sensing material at minute 30. As the sensing material's surface saturates, the steepness of the negative slope diminishes, but remains negative at 40 min. If we consider for time response, the time to reach 50% of the starting peak-to-valley value, then again, we can see about the same value. In our testing cycle, at minute 40 the methane is stopped, and the recovery process begins, and evolves until minute 50. Disregarding the signal's noise, we can observe an almost complete recovery of the signal to the starting value from minute 30. This way, one can estimate a time to full recovery of about 10 min. The time to 50% recovery is around 2.5–3 min only, since the recovery is also not linear.

After the recovery times, the response returns to almost the same value as in the absence of gas. This point forms the basis for the high degree of reversibility of the proposed device.

It is worth noting that this nanocomposite shows also a modest response to methane already from a concentration as low as 100 ppm, but the magnitude of the sensing material's response at

1000 ppm, presented above in Figures 10 and 11, is much better. At this stage it is suitable for signaling gas presence, before reaching the critical LEL concentration of methane at 50,000 ppm [73]. Industrial environments and mining sectors involving methane presence might benefit from the further development of such a threshold sensing material for early warning.

3. Discussion

SnSe₂ has a layered structure, consisting of triple-layer units, where the Sn layer sits between two Se layers [74]. In this way, the triple-layer units will face toward the neighboring next unit through Se atoms. Due to the lone pair electrons of the Se atoms, it seems plausible to admit that the electron density is higher in these Se-Se sheet-like interfaces, compared to the inner volume of the triple-layer unit, which includes the Sn sheet. We consider that this modulated electron density feature will support the electrical response of the SnSe₂ during the gas sensing process, through the available electrons in these interface volumes. Further on, we tried to enhance the electrical responsivity of SnSe₂ by making the nanocomposite material of SnSe₂ and ZnTAPP, knowing the remarkable properties of the Zn-porphyrins [75,76].

As a general chemical behavior, zinc porphyrins have a pentadentate coordination mode [36], which allowed only one more axial ligand to be complexed to the zinc atom (possessing a close *d* shell) in the center of porphyrin. Nevertheless, it was demonstrated in [36] that several zinc porphyrins can become six-coordinate, binding in solution two axial ligands (for example pyridine), if the resulting complex is suitably stabilized by chelation.

The influence of the central metal—especially its radius, electrostatic attraction and steric effects on the properties of porphyrins, as well as the influence of the used solvent were deeply investigated [77], taking into consideration that in solvated porphyrins the solvent molecules cause the distortion of the ring skeleton, and thus reducing the porphyrin's symmetry. So, even in solution, the ability of zinc porphyrins to form six-fold coordination complexes is extremely limited and an increased distortion in porphyrin conformation is not an indication of an enhanced interaction.

Thus, it is more likely that the zinc porphyrin prefer to link only one axial ligand, being more performant when the concentration of the gas is low, as revealed in this study.

Based on Pearson's principle [78], a strong interaction can be possible between two hard (i.e., weakly polarizable) or two soft (i.e., highly polarizable) Lewis' bases and acids. Thus, the volatile molecules that possess lone pairs of electrons, such as alcohols and amines, favor axial coordination with the zinc porphyrins, this effect being prevalent over hydrogen bonding formation [79]. As a consequence, in Zn-porphyrins the binding energy is increased by the weakly electron donating carbon atoms, such as methane. The exposure of the film to the CH₄ gas will lead to distortion of molecules, ending with returning to the monomeric state when the concentration of CH₄ is high [80].

In the presence of humidity, the sensing is more difficult, because water molecules compete with CH₄ gas for the coordination site. Taking into consideration the methodology used to prepare our sensor, the CH₄ analyte might interact with both the porphyrin, and the SnSe₂ semiconductor. Even so, we consider that the sensitivity of the sensor is mainly due to the interaction with the porphyrins, because it is known that the conductivity of porphyrins, surrounded by SnSe₂ semiconductors, is influenced by adsorbed molecules that also affect the extended π - π delocalization, decreasing it in this way [72].

Zinc porphyrin molecules are usually acting as electron donors, while SnSe₂ is known to present structural polytypes, which determines its n or p type conduction [81–84].

The surface of the sensing nanocomposite layer, exposed to the analyzed gas, able to get in contact with its molecules, is mostly formed from Se atoms from the edges of the–Se–Sn–Se–layer stacks, or from the central Zn atoms of the Zn-porphyrin molecules, forming practically an electron-rich surface.

In our present understanding, the complex structure of our nanocomposite, and the results we have so far, makes it difficult to propose a comprehensive and plausible sensing mechanism. However, we think that the interplay between the layer-like structures of both the SnSe₂ and the

Zn-prophyrin, the lone-pair electrons of the Se, and the electronegativity values of each kind of the interacting atoms have an important role in this sensing mechanism.

The gas sensing mechanism was previously described [27] as related to the charge transfer (decreasing in carrier concentration) and the flat band (reducing in the mobility) induced by gas adsorption. The electron-donating character of CH₄ is specifically indicated. We might further point out the fact that direct transfer (physisorption) of electrons from CH₄ occurs at low temperatures with less ability of charge transfer.

One major argument is that only chalcogenide atoms are associated with Lone-Pair (LP) states. The energy of LP states strongly depends on the chemical environment, so LP electrons close to electropositive atoms and donor electron effect molecules (such as CH₄) will have higher energy than those near electronegative atoms, having a withdrawing electron effect. So donor electron effect molecules, such as CH₄, will raise some LP states into the gap, thus enlarging the valence band tail. On the other hand, it is well known that higher Se concentration determines LP band to become the valence band. This behavior of SnSe₂ is strongly potentiated by the ZnTAPP that, due to its four NH₂ substituent groups, is additionally increasing the donor electron effect on the chalcogenide atoms.

Based on these, we can presume that methane sensing is dependent upon the above mentioned compositional disordering, meaning that conductivity is achieved in this case mainly by hopping between localized states in the extended band tails [84].

4. Conclusions

We obtained a new nanocomposite based on SnSe₂ and ZnTAPP as drop-casted thin films. These thin films proved to be sensitive to methane (CH₄) in concentrations as low as 1000 ppm, at a room temperature of about 25 °C, without the need of heating the sensing element. Since for methane there are known [85] the lower explosion limit (LEL) concentration of 5 vol%, corresponding to 50,000 ppm, and the upper explosion limit (UEL) of 15 vol%, corresponding to a concentration of 150,000 ppm, the nanocomposite material proposed by us here and in [26], allows for an early warning if methane might be present in a given monitored area. Table 1 presents data enabling the comparison of the methane sensing performance of our new nanocomposite with other methane sensitive materials.

Table 1. Detection limits and linear concentration range of recently developed sensors for the determination of methane, using different sensitive materials and methods.

Sensitive Material	Detection Method	Linear Concentration Range (ppm)	Detection Limit (ppm, ppb)	Reference
Dual-gas quartz-enhanced photoacoustic (QEPAS) sensor	Diode laser and a quantum cascade laser	-	18 ppb for CH ₄ , 5 ppb for N ₂ O and 20 ppm for water vapor	[85]
Graphene electrodes decorated with palladium NPs	Electrooxidation of methane to CO ₂	1 to 50 ppm	9 ppm	[86]
Optical Gas Imaging Technologies	Passive infrared (IR) imaging	1 g/s to 21 g/s Leak size	-	[87]
A reference Ag layer, adhesion layer, a Nafion layer and two interdigitated Pt electrodes all on top of a Si/SiO ₂ substrate.	Cyclic Voltammetry	Detect methane dissolved in N ₂ from 10% to 50%	10% CH ₄ in N ₂	[88]
Chelating Phosphine Ligand Stabilized AuNPs	Chemiresistive methane detection	200 ppm to 1000 ppm	100 ppm at 80 °C	[89]
Mini-multi-pass cell with a 4.2 m optical path length using two common spherical mirrors	Tunable diode laser absorption spectroscopy	1.98 to 9.28 ppm	117 ppb	[90]
Graphene Decorated with Silver Nanoparticles	Electrical resistance measurements	400–20000 ppm at room temperature	-	[91]
PdPt Bimetal-Functionalized SnO ₂ Nanosheets	Electrical resistance measurements	-	500 ppm of CH ₄ at 320 °C	[17]
Thin films of SnSe ₂ -Zn-porphyrin	Electrical resistance measurements	-	1000 ppm at room temperature 23–28 °C	<i>This work</i>

We have checked for the reproducibility of the sensor's response to methane in dry air with other sensors, made in the same way. The peak-to-valley amplitude, as well as the global tendency in response (i.e., the decrease in the presence of methane, increase without methane), was also the same.

Even if the magnitude of the resistive response of this new nanocomposite thin film is not as large as those of other classical sensors, the fact that it works at room temperature, without the need of a heating element, makes it a good choice to be considered for further sensor development. At this stage it is suitable for signaling gas presence before reaching the critical lower explosion limit (LEL) concentration threshold of methane at 50,000 ppm [84]. Industrial environments and mining sectors involving methane presence could benefit from the further development of such a threshold sensing material for early warning.

Author Contributions: A.L. proposed the subject of the study, wrote a first draft of the manuscript and supervised the inputs of the co-authors; E.F.-C. contributed with conception and design of the porphyrins involved in the study, and provided specific characterization of them, along with manuscript writing; G.S. established the protocol and supervised the gas sensing measurements, while A.M. performed these measurements, and contributed to specific literature update and manuscript revision; E.M. performed the SEM study of the selected samples; F.S. and A.L. have done the XRD measurements, diagram indexing and interpretation, while M.Ş. performed the ESR spectroscopy measurements and interpretations. All authors have read and agreed to the published version of the manuscript.

Funding: This research has been supported by the Romanian Ministry of Education, Core Program 21N/2019, and by Romanian Academy, through Research Programme Nr. 3/2020 at the Institute of Chemistry Timisoara.

Conflicts of Interest: The authors declare no conflict of interest with the research performed and reported here.

References

- Seiyama, T.; Kato, A.; Fujiishi, K.; Nagatani, M. A new detector for gaseous components using semiconductive thin films. *Anal. Chem.* **1962**, *34*, 1502–1503. [CrossRef]
- Yamazoe, N. New approaches for improving semiconductor gas sensors. *Sens. Actuators B Chem.* **1991**, *5*, 7–19. [CrossRef]
- Marian, S.; Potje-Kamloth, K.; Tsyulyanu, D.; Liess, H.D. Dimorphite based gas sensitive thin films. *Thin Solid Films* **2000**, *359*, 108. [CrossRef]
- Tsiuleanu, D.; Marian, S.; Potje-Kamloth, K.; Liess, H.D. Verwendung von Chemisch Sensitiven Chalkogenen und Chalkogeniden zur Detektion von gas- und Dampfförmigen Analyten in Gasen. DE Patent No. DE 100 19010 A1, 25 October 2001.
- Mitzi, D.B. Solution Deposition of Chalcogenide Films. U.S. Patent No. 6,875,661, 4 May 2005.
- Liu, H.F.; He, Q.X.; Zheng, C.T.; Wang, Y.D. Development of a portable mid-infrared methane detection device. *Optoelectron. Lett.* **2017**, *13*, 100–103. [CrossRef]
- Ma, H.Y.; Qin, S.L.; Wang, L.Y.; Wang, G.; Zhao, X.H.; Ding, E.J. The study on methane sensing with high-temperature low-power CMOS compatible silicon microheater. *Sens. Actuators B Chem.* **2017**, *244*, 17–23. [CrossRef]
- Bărsan, N.; Tomescu, A. The temperature dependence of the response of SnO₂-based gas sensing layers to O₂, CH₄ and CO. *Sens. Actuators B Chem.* **1995**, *26*, 45–48. [CrossRef]
- Sberveglieri, G. (Ed.) *Gas Sensors*; Kluwer Academic Publishers: Dordrecht, The Netherlands, 1992.
- Schierbaum, K.D.; Weimar, U.; Gopel, W. Comparison of ceramic thick-film and thin-film chemical sensors based upon SnO₂. *Sens. Actuators B Chem.* **1992**, *7*, 709–716. [CrossRef]
- Amutha, A.; Amirthapandian, S.; Prasad, A.K.; Panigrahi, B.K.; Thangadurai, P. Methane gas sensing at relatively low operating temperature by hydrothermally prepared SnO₂ nanorods. *J. Nanopart. Res.* **2015**, *17*, 289. [CrossRef]
- Fedorenko, G.; Oleksenko, L.; Maksymovych, N.; Skolyar, G.; Ripko, O. Semiconductor gas sensors based on Pd/SnO₂ nanomaterials for methane detection in air. *Nanoscale Res. Lett.* **2017**, *12*, 329. [CrossRef]
- Mitra, P.; Mukhopadhyay, A.K. ZnO thin film as methane detection sensor. *Bull. Pol. Acad. Tech.* **2007**, *55*, 281–285. Available online: <http://cgcri.csircentral.net/id/eprint/510> (accessed on 16 November 2020).

14. Bhattacharyya, P.; Basu, P.K.; Lang, C.; Saha, H.; Basu, S. Noble metal catalytic contacts to sol-gel nanocrystalline zinc oxide thin films for sensing of methane. *Sens. Actuators B Chem.* **2008**, *129*, 551–557. [CrossRef]
15. Ghosh, S.; RoyChaudhury, C.; Bhattacharyya, R.; Saha, H.; Mukherjee, N. Palladium-Silver-Activated ZnO surface: Highly selective methane sensor at reasonably low operating temperature. *ACS Appl. Mater. Interfaces* **2014**, *6*, 3879–3887. [CrossRef]
16. Wu, Z.; Chen, X.; Zhu, S.; Zhou, Z.; Yao, Y.; Quan, W.; Liu, B. Room temperature methane sensor based on graphene nanosheets/polyaniline nanocomposite thin film. *IEEE Sens. J.* **2013**, *13*, 777–782. [CrossRef]
17. Ghanbari, R.; Safaiee, R.; Sheikhi, M.H.; Golshan, M.M.; Karami Horastani, Z. Graphene decorated with silver nanoparticles as a low-temperature methane gas sensor. *ACS Appl. Mater. Interfaces* **2019**, *11*, 21795–21806. [CrossRef]
18. Lam, K.C.; Huang, B.; Shi, S.Q. Room-temperature methane gas sensing properties based on in situ graphene oxide incorporated with tin oxide. *J. Mater. Chem. A* **2017**, *5*, 11131–11142. [CrossRef]
19. Wang, T.; Huang, D.; Yang, Z.; Xu, S.; He, G.; Li, X.; Hu, N.; Yin, G.; He, D.; Zhang, L. A review on graphene-based gas/vapor sensors with unique properties and potential applications. *Nano Micro Lett.* **2016**, *8*, 95–119. [CrossRef]
20. Yang, N.; Yang, D.; Chen, L.; Liu, D.; Cai, M.; Fan, X. A novel interconnected structure of graphene-carbon nanotubes for the application of methane adsorption. *IEEE Sens. J.* **2018**, *18*, 1555–1561. [CrossRef]
21. Devkota, J.; Kim, K.J.; Ohodnicki, P.R.; Culp, J.T.; Greve, D.W.; Lekse, J.W. Zeolitic imidazolate framework-coated acoustic sensors for room temperature detection of CO₂ and CH₄. *Nanoscale* **2018**, *10*, 8075–8087. [CrossRef]
22. Cao, R.; Ding, H.; Peng, Z.; Kim, K.J.; Ohodnicki, P.; Yan, A.; Chen, K.P. Fiber optical sensor for methane detection based on metal-organic framework/silicone polymer coating. In Proceedings of the IEEE Xplore, Conference on Lasers and Electro-Optics (CLEO), San Jose, CA, USA, 13–18 May 2018; p. 8427422.
23. Cardenas, J.C.; Castillo, L.A.; Molano, W.; Reiber, A.; Sierra, C.A. Fluorescent post-synthetic modified MOFs for methane sensing. *TechConnect Briefs* **2016**, *2*, 88–91.
24. Tian, T.; Zeng, Z.; Vulpe, D.; Casco, M.E.; Divitini, G.; Midgley, P.A.; Silvestre-Albero, J.; Tan, J.C.; Moghadam, P.Z.; Fairen-Jimenez, D. A sol-gel monolithic metal-organic framework with enhanced methane uptake. *Nat. Mater.* **2017**, *17*, 174–179. [CrossRef]
25. Zeitler, T.R.; Allendorf, M.D.; Greathouse, J.A. Grand canonical Monte Carlo simulation of low pressure methane adsorption in nanoporous framework materials for sensing applications. *J. Phys. Chem. C* **2012**, *116*, 3492–3502. [CrossRef]
26. Lőrinczi, A.; Făgădar-Cosma, E.; Socol, G.; Mihăilescu, A.; Matei, E.; Ștefan, M.; Logofătu, C. Methane Sensitive Material at Room Temperature. RO Patent Request No. A/00621/29.08.2018. Available online: https://osim.ro/wp-content/uploads/Publicatii-OSIM/BOPI-Inventii/2019/bopi_inv_01_2019.pdf (accessed on 15 December 2020).
27. Camargo Moreira, Ó.L.; Cheng, W.-Y.; Fuh, H.-R.; Chien, W.-C.; Yan, W.; Fei, H.; Xu, H.; Zhang, D.; Chen, Y.; Zhao, Y.; et al. High Selectivity Gas Sensing and Charge Transfer of SnSe₂. *ACS Sens.* **2019**, *4*, 2546–2552. [CrossRef] [PubMed]
28. Paolucci, V.; D'Olimpio, G.; Kuo, C.-N.; Lue, C.S.; Boukhvalov, W.; Cantalini, C.; Politano, A. Self-Assembled SnO₂/SnSe₂ Heterostructures: A Suitable Platform for Ultrasensitive NO₂ and H₂ Sensing. *ACS Appl. Mater. Interfaces* **2020**, *12*, 34362–34369. [CrossRef] [PubMed]
29. Popescu, M.; Sava, F.; Lőrinczi, A.; Socol, G.; Mihăilescu, I.N.; Tomescu, A.; Simion, C. Structure, properties and gas sensing effect of SnSe₂ films, prepared by pulsed laser deposition method. *J. Non-Cryst. Solids* **2007**, *353*, 1865–1869. [CrossRef]
30. Popescu, M.; Sava, F.; Lőrinczi, A.; Tomescu, A.; Simion, C.; Socol, G.; Mihailescu, I.N.; Miclos, S.; Savastru, D. Methane-Sensitive Material and Threshold Sensor for Methane Detection. RO Patent No. RO 123461-B1, 29 June 2012.
31. Assili, K.; Gonzalez, O.; Alouani, K.; Vilanova, X. Structural, morphological, optical and sensing properties of SnSe and SnSe₂ thin films as a gas sensing material. *Arab. J. Chem.* **2020**, *13*, 1229–1246. [CrossRef]
32. Chen, M.; Li, Z.; Li, W.; Shan, C.; Li, W.; Li, K.; Gu, G.; Feng, Y.; Zhong, G.; Wei, L.; et al. Large-scale synthesis of single-crystalline self-standing SnSe₂ nanoplate arrays for wearable gas sensors. *Nanotechnology* **2018**, *29*, 455501. [CrossRef]

33. Di Natale, C.; Monti, D.; Paolesse, R. Chemical sensitivity of porphyrin assemblies. *Mater. Today* **2010**, *13*, 46–52. [[CrossRef](#)]
34. Lvova, L.; Di Natale, C.; Paolesse, R. Porphyrin-based chemical sensors and multisensor arrays operating in the liquid phase. *Sens. Actuators B Chem.* **2013**, *179*, 21–31. [[CrossRef](#)]
35. Paolesse, R.; Lvova, L.; Nardis, S.; Di Natale, C.; D'Amico, A.; Lo Castro, F. Chemical images by porphyrin arrays of sensors. *Microchim. Acta* **2008**, *163*, 103–112. [[CrossRef](#)]
36. Monti, D.; Nardis, S.; Stefanelli, M.; Paolesse, R.; Di Natale, C.; D'Amico, A. Porphyrin-Based Nanostructures for Sensing Applications. *J. Sens.* **2009**, *2009*, 856053. [[CrossRef](#)]
37. Paolesse, R.; Nardis, S.; Monti, D.; Stefanelli, M.; Di Natale, C. Porphyrinoids for Chemical Sensor Applications. *Chem. Rev.* **2017**, *117*, 2517–2583. [[CrossRef](#)] [[PubMed](#)]
38. Ngo, H.T.; Minami, K.; Imamura, G.; Shiba, K.; Yoshikawa, G. Effects of Center Metals in Porphines in Nanomechanical Gas Sensing. *Sensors* **2018**, *18*, 1640. [[CrossRef](#)] [[PubMed](#)]
39. Osica, I.; Imamura, G.; Shiba, K.; Ji, Q.; Shrestha, L.K.; Hill, J.P.; Kurzydłowski, K.J.; Yoshikawa, G.; Ariga, K. Highly Networked Capsuled Silica-Porphyrin Hybrid Nanostructures as Efficient Materials for Acetone Vapor Sensing. *ACS Appl. Mater. Interfaces* **2017**, *9*, 9945–9954. [[CrossRef](#)] [[PubMed](#)]
40. Lascu, A.; Palade, A.; Fagadar-Cosma, G.; Creanga, I.; Ianasi, C.; Sebarchievici, I.; Birdeanu, M.; Fagadar-Cosma, E. Mesoporous manganese-porphyrin-silica hybrid nanomaterial sensitive to H₂O₂ fluorescent detection. *Mater. Res. Bull.* **2016**, *74*, 325–332. [[CrossRef](#)]
41. Popescu, M.; Simandan, I.D.; Sava, F.; Velea, A.; Fagadar-Cosma, E. Sensor of Nitrogen Dioxide Based on Single Wall Carbon Nanotubes and Manganese-Porphyrin. *Dig. J. Nanomater. Biostruct.* **2011**, *6*, 1253–1256.
42. Wang, Y.; Akhigbe, J.; Ding, Y.; Brueckner, C.; Lei, Y. Meso-Tritolylcorrole-Functionalized Single-walled Carbon Nanotube Donor-Acceptor Nanocomposites for NO₂ Detection. *Electroanalysis* **2012**, *24*, 1348–1355. [[CrossRef](#)]
43. Liu, S.F.; Moh, L.C.H.; Swager, T.M. Single-Walled Carbon Nanotube–Metalloporphyrin Chemiresistive Gas Sensor Arrays for Volatile Organic Compounds. *Chem. Mater.* **2015**, *27*, 3560–3563. [[CrossRef](#)]
44. Penza, M.; Rossi, R.; Alvisi, M.; Signore, M.A.; Serra, E.; Paolesse, R.; D'Amico, A.; Di Natale, C. Metalloporphyrins-modified carbon nanotubes networked films-based chemical sensors for enhanced gas sensitivity. *Sens. Actuators B Chem.* **2010**, *144*, 387–394. [[CrossRef](#)]
45. Penza, M.; Alvisi, M.; Rossi, R.; Serra, E.; Paolesse, R.; D'Amico, A.; Di Natale, C. Carbon nanotube films as a platform to transduce molecular recognition events in metalloporphyrins. *Nanotechnology* **2011**, *22*, 125502. [[CrossRef](#)]
46. Saxena, S.; Verma, A.L. Metal-tetraphenylporphyrin functionalized carbon nanotube composites as sensor for benzene, toluene and xylene vapors. *Adv. Mater. Lett.* **2014**, *5*, 472–478. [[CrossRef](#)]
47. Saxena, S.; Saini, G.S.S.; Verma, A.L. Co-TPP functionalized carbon nanotube composites for detection of nitrobenzene and chlorobenzene vapours. *Bull. Mater. Sci.* **2015**, *38*, 443–449. [[CrossRef](#)]
48. Shirsat, M.D.; Sarkar, T.; Kakoullis, J.; Myung, N.V.; Konnanath, B.; Spanias, A.; Mulchandani, A. Porphyrin-Functionalized Single-Walled Carbon Nanotube Chemiresistive Sensor Arrays for VOCs. *J. Phys. Chem. C* **2012**, *116*, 3845–3850. [[CrossRef](#)] [[PubMed](#)]
49. Rushi, A.; Datta, K.; Ghosh, P.; Mulchandani, A.; Shirsat, M.D. Iron tetraphenylporphyrin functionalized single wall carbon nanotubes for the detection of benzene. *Mater. Lett.* **2013**, *96*, 38–41. [[CrossRef](#)]
50. Sarkar, T.; Srinives, S.; Sarkar, S.; Haddon, R.C.; Mulchandani, A. Single-Walled Carbon Nanotube-Poly(porphyrin) Hybrid for Volatile Organic Compounds Detection. *J. Phys. Chem. C* **2014**, *118*, 1602–1610. [[CrossRef](#)]
51. Fagadar-Cosma, E.; Tarabukina, E.; Zakharova, N.; Birdeanu, M.; Taranu, B.; Palade, A.; Creanga, I.; Lascu, A.; Fagadar-Cosma, G. Hybrids formed between poly-vinylpyrrolidone and an A₃B porphyrin dye: Behaviour in aqueous solutions and chemical response to CO₂ presence. *Polym. Int.* **2016**, *65*, 200–209. [[CrossRef](#)]
52. Mak, C.A.; Pericas, M.A.; Fagadar-Cosma, E. Functionalization of A₃B-type porphyrin with Fe₃O₄ MNPs. Supra-molecular assemblies, gas sensor and catalytic applications. *Catal. Today* **2018**, *306*, 268–275. [[CrossRef](#)]
53. Fagadar-Cosma, E.; Vlascici, D.; Fagadar-Cosma, G.; Palade, A.; Lascu, A.; Creanga, I.; Birdeanu, M.; Cristescu, R.; Cernica, I. A Sensitive A₃B Porphyrin Nanomaterial for CO₂ Detection. *Molecules* **2014**, *19*, 21239–21252. [[CrossRef](#)]

54. Fagadar-Cosma, E.; Badea, V.; Fagadar-Cosma, G.; Palade, A.; Lascu, A.; Fringu, I.; Birdeanu, M. Trace Oxygen Sensitive Material Based on Two Porphyrin Derivatives in a Heterodimeric Complex. *Molecules* **2017**, *22*, 1787. [CrossRef]
55. Garg, K.; Singh, A.; Debnath, A.K.; Nayak, S.K.; Chattopadhyay, S.; Aswal, D.K.; Hayakawa, Y.; Gupta, S.K.; Yakhmi, J.V. Bis-porphyrin films as ppb level chemiresistive sensors. *Chem. Phys. Lett.* **2010**, *488*, 27–31. [CrossRef]
56. Garg, K.; Singh, A.; Majumder, C.; Nayak, S.K.; Aswal, D.K.; Gupta, S.K.; Chattopadhyay, S. Room temperature ammonia sensor based on jaw like bis-porphyrin molecules. *Org. Electron.* **2013**, *14*, 1189–1196. [CrossRef]
57. Park, J.H.; Ko, J.H.; Hong, S.; Shin, Y.J.; Park, N.; Kang, S.; Lee, S.M.; Kim, H.J.; Son, S.U. Hollow and Microporous Zn-Porphyrin Networks: Outer Shape Dependent Ammonia Sensing by Quartz Crystal Microbalance. *Chem. Mater.* **2015**, *27*, 5845–5848. [CrossRef]
58. Colombelli, A.; Manera, M.G.; Borovkov, V.; Giancane, G.; Valli, L.; Rella, R. Enhanced sensing properties of cobalt bis-porphyrin derivative thin films by a magneto-plasmonic-opto-chemical sensor. *Sens. Actuators B Chem.* **2017**, *246*, 1039–1048. [CrossRef]
59. Çapan, I.; Ozkaya, C. Characterization of Octaethyl Porphyrin Thin Films with Application to Determination of Volatile Organic Compounds. *Anal. Lett.* **2016**, *49*, 423–432. [CrossRef]
60. Çapan, İ.; Erdoğan, M.; Güner, B.; İlhan, B.; Stanciu, S.G.; Hristu, R.; Stanciu, G.A. Gas Sensing Properties of Porphyrin Thin Films Influenced by Their Surface Morphologies. *Sens. Lett.* **2014**, *12*, 1218–1227. [CrossRef]
61. Guillen, M.G.; Gamez, F.; Roales, J.; Lopes-Costa, T.; Pinto, S.M.A.; Calvete, M.J.F.; Pereira, M.M.; Pedrosa, J.M. Molecular-based selection of porphyrins towards the sensing of explosives in the gas phase. *Sens. Actuators B Chem.* **2018**, *260*, 116–124. [CrossRef]
62. Garcia-Berrios, E.; Theriot, J.C.; Woodka, M.D.; Lewis, N.S. Detection of ammonia, 2,4,6-trinitrotoluene, and common organic vapors using thin-film carbon black-metallo-porphyrin composite chemiresistors. *Sens. Actuators B Chem.* **2013**, *188*, 761–767. [CrossRef]
63. Bettelheim, A.; White, B.A.; Raybuck, S.A.; Murray, R.W. Electrochemical polymerization of amino-, pyrrole-, and hydroxy- substituted tetraphenylporphyrins. *Inorg. Chem.* **1987**, *26*, 1009–1017. [CrossRef]
64. Araghi, M.; Mirkhani, V.; Moghadam, M.; Tangestaninejad, S.; Mohammadpoor-Baltork, I. Synthesis and characterization of a new porphyrin-polyoxometalate hybrid material and investigation of its catalytic activity. *Dalton Trans.* **2012**, *41*, 3087–3094. [CrossRef]
65. Stoll, S.; Schweiger, A. EasySpin, a comprehensive software package for spectral simulation and analysis in EPR. *J. Magn. Reson.* **2006**, *178*, 42–55. [CrossRef]
66. Vhadlure, A.N.; Rohikar, R.V.; Kulkarni, G.A.; Suryavanshi, A.W.; Mathkari, S.S.; Mathapati, S.R. Synthesis and Spectral Characterization of Substituted Tetraphenylporphyrin Iron Chloride Complexes. *Int. J. Chem. Tech. Res.* **2013**, *5*, 522–527.
67. Nguyen, T.N.; Håkansson, P.; Edge, R.; Collison, D.; Goodman, B.A.; Burns, J.R.; Stulz, E. EPR based distance measurement in Cu-porphyrin-DNA. *New J. Chem.* **2014**, *38*, 5254–5259. [CrossRef]
68. McQuarters, A.B.; Goodrich, L.E.; Goodrich, C.M.; Lehnert, N. Disproportionation of O-Benzylhydroxylamine Catalyzed by a Ferric Bis-Picket Fence Porphyrin Complex. *Z. Anorg. Allg. Chem.* **2013**, *639*, 1520–1526. [CrossRef]
69. Askhabov, A.M.; Yushkin, N.P. The kvataron mechanism responsible for the genesis of noncrystalline forms of nanostructures. *Doklady Earth Sci.* **1999**, *368*, 940–942.
70. Sakka, S.; Kozuka, H. (Eds.) *Handbook of Sol-Gel Science and Technology. 1. Sol-Gel Processing*; Kluwer Academic Publishers: Osaka, Japan, 2005; p. 228.
71. Nardis, S.; Pomarico, G.; Tortora, L.; Capuano, R.; D'Amico, A.; Di Natale, C.; Paolesse, R. Sensing mechanisms of supramolecular porphyrin aggregates: A teamwork task for the detection of gaseous analytes. *J. Mater Chem.* **2011**, *21*, 18638–18644. [CrossRef]
72. Magna, G.; Dinc Zor, S.; Catini, A.; Capuano, R.; Basoli, F.; Martinelli, E.; Paolesse, R.; Di Natale, C. Surface arrangement dependent selectivity of porphyrins gas sensors. *Sens. Actuators B Chem.* **2017**, *251*, 524–532. [CrossRef]
73. Lower and Upper Explosive Limits for Flammable Gases and Vapors (LEL/UEL). Available online: [https://www.mathesongas.com/pdfs/products/Lower-\(LEL\)-&-Upper-\(UEL\)-Explosive-Limits-.pdf](https://www.mathesongas.com/pdfs/products/Lower-(LEL)-&-Upper-(UEL)-Explosive-Limits-.pdf) (accessed on 25 October 2020).

74. Zeng, J.; Liu, E.; Fu, Y.; Chen, Z.; Pan, C.; Wang, C.; Wang, M.; Wang, Y.; Xu, K.; Cai, S.; et al. Gate-Induced Interfacial Superconductivity in 1T-SnSe₂. *Nano Lett.* **2018**, *18*, 1410–1415. [CrossRef]
75. Rushi, D.; Datta, K.P.; Ghosh, P.; Mulchandani, A.; Shirsat, M.D. Exercising substituents in porphyrins for real time selective sensing of volatile organic compounds. *Sens. Actuators B Chem.* **2018**, *257*, 389–397. [CrossRef]
76. Favereau, L.; Cnossen, A.; Kelber, J.B.; Gong, J.Q.; Oetterli, R.M.; Cremers, J.; Herz, L.M.; Anderson, H.L. Six-Coordinate Zinc-Porphyrins for Template-Directed Synthesis of Spiro-Fused Nanorings. *J. Am. Chem. Soc.* **2015**, *137*, 14256–14259. [CrossRef]
77. Schalk, O.; Liang, Y.; Unterreiner, A.N. On Ligand Binding Energies in Porphyrinic Systems. *Z. Phys. Chem.* **2013**, *227*, 35–47. [CrossRef]
78. Pearson, R.G. Hard and Soft Acids and Bases. *J. Am. Chem. Soc.* **1963**, *85*, 3533. [CrossRef]
79. Zhuo, C.-C.; Li, L.; Hu, C.-J.; Lang, J.-P. Host-guest assembly for highly sensitive probing of a chiral mono-alcohol with a zinc trisphosphorylate. *Sci. Rep.* **2017**, *7*, 3829. [CrossRef]
80. Ray, P.C.; Leszczynski, J. Nonlinear optical properties of highly conjugated push-pull porphyrin aggregates: Role of intermolecular interaction. *Chem. Phys. Lett.* **2006**, *419*, 578. [CrossRef]
81. Tracy, B.D.; Li, X.; Liu, X.; Furdyna, J.; Dobrowolska, M.; Smith, D.J. Characterization of structural defects in SnSe₂ thin films grown by molecular beam epitaxy on GaAs (111)B substrates. *J. Cryst. Growth* **2016**, *453*, 58–64. [CrossRef]
82. Yu, P.; Yu, X.C.; Lu, W.L.; Lin, H.; Sun, L.F.; Du, K.; Liu, F.; Fu, W.; Zeng, Q.; Shen, Z.; et al. Fast Photoresponse from 1T Tin Diselenide Atomic Layers. *Adv. Funct. Mater.* **2016**, *26*, 137–145. [CrossRef]
83. Busch, G.; Fröhlich, C.; Hulliger, F.; Steigmeier, E. Struktur, elektrische und thermoelektrische Eigenschaften von SnSe₂. *Helv. Phys. Acta* **1961**, *34*, 359–368. [CrossRef]
84. Bletskan, D.I. Phase Equilibrium in Binary Systems A^{IV}B^{VI}. *J. Ovonic Res.* **2005**, *1*, 61–69. Available online: <https://chalcogen.ro/Bletskan2.pdf> (accessed on 29 October 2020).
85. Tsiulyanu, D. Gas-sensing features of nanostructured tellurium thin films. *Beilstein J. Nanotechnol.* **2020**, *11*, 1010–1018. [CrossRef]
86. Elefante, A.; Giglio, M.; Sampaolo, A.; Menduni, G.; Patimisco, P.; Passaro, V.M.N.; Wu, H.; Rossmadl, H.; Mackowiak, V.; Cable, A.; et al. Dual-Gas Quartz-Enhanced Photoacoustic Sensor for Simultaneous Detection of Methane/Nitrous Oxide and Water Vapor. *Anal. Chem.* **2019**, *91*, 12866–12873. [CrossRef] [PubMed]
87. Dosi, M.; Lau, I.; Zhuang, Y.; Simakov, D.S.A.; Fowler, M.W.; Pope, M.A. Ultrasensitive Electrochemical Methane Sensors Based on Solid Polymer Electrolyte-Infused Laser-Induced Graphene. *ACS Appl. Mater. Interfaces* **2019**, *11*, 6166–6173. [CrossRef]
88. Ravikumar, A.P.; Wang, J.; Brandt, A.R. Are Optical Gas Imaging Technologies Effective for Methane Leak Detection? *Environ. Sci. Technol.* **2017**, *51*, 718–724. [CrossRef]
89. Gross, P.-A.; Jaramillo, T.; Pruitt, B. Cyclic-Voltammetry-Based Solid-State Gas Sensor for Methane and Other VOC Detection. *Anal. Chem.* **2018**, *90*, 6102–6108. [CrossRef] [PubMed]
90. Tang, C.; Ku, K.H.; Lennon Luo, S.-X.; Concellón, A.; Wu, Y.-C.M.; Lu, R.-Q.; Swager, T.M. Chelating Phosphine Ligand Stabilized AuNPs in Methane Detection. *ACS Nano* **2020**, *14*, 11605–11612. [CrossRef] [PubMed]
91. Cui, R.; Dong, L.; Wu, H.; Ma, W.; Xiao, L.; Jia, S.; Chen, W.; Tittel, F.K. Three-Dimensional Printed Miniature Fiber-Coupled Multipass Cells with Dense Spot Patterns for ppb-Level Methane Detection Using a Near-IR Diode Laser. *Anal. Chem.* **2020**, *92*, 13034–13041. [CrossRef] [PubMed]

Publisher's Note: MDPI stays neutral with regard to jurisdictional claims in published maps and institutional affiliations.



© 2020 by the authors. Licensee MDPI, Basel, Switzerland. This article is an open access article distributed under the terms and conditions of the Creative Commons Attribution (CC BY) license (<http://creativecommons.org/licenses/by/4.0/>).